

## RESEARCH ARTICLE

# Experimental First-Photon Visualization of Quantum Erasure With Hybrid Entanglement

Wen-Kai Yu<sup>1</sup> | Qing-Yuan Wu<sup>1</sup> | Xiao-Xiao Chen<sup>2</sup> | Juan Huo<sup>3</sup> | Jian Li<sup>1</sup> | Jia-Zhi Yang<sup>1</sup> | An-Ning Zhang<sup>1</sup>

<sup>1</sup>Center for Quantum Technology Research, Key Laboratory of Advanced Optoelectronic Quantum Architecture and Measurement of Ministry of Education, State Key Laboratory of Chips and Systems for Advanced Light Field Display, School of Physics, Beijing Institute of Technology, Beijing, China | <sup>2</sup>School of Physics and Electronics, Yancheng Teachers University, Yancheng, China | <sup>3</sup>Intelligent Science and Technology Academy of CASIC, Beijing, China

**Correspondence:** Wen-Kai Yu ([yuwenkai@bit.edu.cn](mailto:yuwenkai@bit.edu.cn)) | An-Ning Zhang ([anningzhang@bit.edu.cn](mailto:anningzhang@bit.edu.cn))

**Received:** 11 July 2025 | **Revised:** 25 October 2025 | **Accepted:** 20 November 2025

**Keywords:** first-photon imaging | hybrid entanglement | quantum erasure | quantum phenomena visualization

## ABSTRACT

The complementarity principle, as the cornerstone of quantum information, is both counterintuitive and inherently characterized by mutual exclusivity. In this work, we construct a quantum erasure scheme utilizing polarization and orbital angular momentum (OAM) two-photon hybrid entanglement, and develop a first-photon physics-enhanced dual-branch residual attention network with physical constraints to visualize the disappearance and reappearance of single-photon petal-like interference patterns, with much fewer than one photon per pixel and without the need for exhaustive detection of all OAM modes. This work not only helps people to deepen their intuitive understanding of the which-path concept in quantum mechanics, but also advances quantum imaging in the visualization of subtle changing quantum phenomena.

## 1 | Introduction

Complementarity stands as a fundamental principle in quantum mechanics, and wave-particle duality serves as a quintessential manifestation of this concept. Both theoretical [1, 2] and experimental [3, 4] studies have demonstrated that the entanglement between interfering particles and measurement devices underpins the availability of which-path information, which in turn destroys interference. By correlating particles with appropriate measurements performed on the which-path markers, it is possible to erase the which-path information and restore interference—a phenomenon known as quantum erasure [4]. Through quantum erasure, observers can selectively reveal either the particle or wave nature of a quantum system, or even explore a continuous transition between these two properties [5–9]. All these have been experimentally realized in various configurations, particularly through interferometers [3, 10] or

Young's double slits [4], which can be regarded as quantum erasers. The former approach is especially intriguing, as it enables the intrinsic degrees of freedom (DOFs) of photons rather than physical slits to be used as abstract paths [11], offering a versatile platform for studying quantum erasure.

In light of these developments, several studies [10–14] have adopted the orbital angular momentum (OAM) of photons as the quantum eraser, replacing the traditional reliance on physical paths. The OAM [15–18] has garnered significant attention due to its discrete and infinite orthogonal modes in the spatial domain, and it has been extensively utilized in quantum communication [19–23]. And there was a strong expectation that the complementarity between the which-path information could be observed from interference patterns [24] in an OAM-based system, as in traditional double-slit experiments, but previous OAM quantum erasure experiments required mode switching

Wen-Kai Yu, Qing-Yuan Wu, and Xiao-Xiao Chen contributed equally to this work and are co-first authors.

to detect the OAM quantum states. This involved exhaustively detecting all possible modes rather than directly extracting useful information from interference patterns. In our earlier work [25–27], we successfully measured the OAM quantum states using quantum imaging techniques, achieving the detection of finite-dimensional OAM in a single imaging process. But the effectiveness of this approach was limited by the need for a large number of photons to reconstruct the OAM states. Recently, first-photon imaging [28–33] and photon-efficient algorithms [34–36] have shown remarkable capabilities in high-quality imaging with a few photons. Nevertheless, they are highly dependent on laser pulses, rendering them incompatible with continuous wave entangled sources considered here. Meanwhile, deep-learning approaches for OAM-resolved imaging and holography have been shown to work effectively with bright classical beams and stable channels [38–43]; but they are not applicable to the conditions of photon-limited entangled light. Consequently, how to reveal, with far fewer photons, the disappearance and reappearance of petal-like OAM interference in a two-photon hybrid entanglement system remains a key open question for achieving quantum erasure.

In this work, we propose a novel scheme for which-path measurement by using polarization-OAM two-photon hybrid entanglement. A quantized first-photon algorithm is developed to visualize quantum erasure based on the above hybrid entanglement, making an exciting step toward the extension of first-photon algorithms to the field of quantum entanglement. Unlike traditional polarization-OAM entanglement methods [10, 11], our approach constructs inseparable polarization-OAM coupled states for the signal photon, enabling the creation of two independent path markers. Furthermore, we design a quantum eraser in each of two arms to realize which-OAM information erasure for the signal photon. Through experimental validation, we demonstrate the imaging detection of unknown OAM quantum states with an average of fewer than one photon per pixel, eliminating the need for exhaustive OAM mode detection. Thus, this approach presents a significant advantage in the efficient utilization of entangled photons. In image reconstruction, we establish a neural network that leverages physical constraints extracted from the fourth time-of-flight histogram dimension to greatly enhance the visibility. This work not only offers a new intuitive perspective for understanding the which-path concept in quantum mechanics, but also provides universal inspirations for quantum imaging with photon limits and its applications in observing subtle changes in physical processes.

## 2 | Theoretical Framework

The transverse spatial distribution of OAM modes is well-characterized by an azimuthal phase in terms of  $e^{im\phi}$  such that a photon can carry an angular momentum of  $\pm mh$ . The integer  $m$  denotes the twist or helicity of the phase profile. For an in-depth study of OAM quantum state erasure, and to provide more degrees of freedom for erasure operations, we consider a polarization-OAM two-photon hybrid entangled state, expressed as the following coherent superposition:

$$|\Psi\rangle_{12} = \frac{1}{\sqrt{2}}(|-mH\rangle_1|V\rangle_2 + |mV\rangle_1|H\rangle_2) \quad (1)$$

where the subscripts 1 and 2 label the entangled photons,  $H$  and  $V$  denote their horizontal and vertical polarizations. By placing a linear polarizer (labeled as polarizer 2) exclusively in the path of photon 2, we can project its state onto:

$$|\theta_2\rangle_2 = \cos\theta_2|H\rangle_2 + \sin\theta_2|V\rangle_2 \quad (2)$$

Since photon 1 encodes both polarization and OAM information, it does not collapse into the superposition state of pure OAM modes  $\{|m\rangle, |-m\rangle\}$  (independent of  $\{|H\rangle_1, |V\rangle_1\}$ ) when an inner product is performed with photon 2, regardless of the angle chosen for polarizer 2. For instance, if photon 2 is projected onto the basis states  $|\theta_2\rangle_2$ , then:

$$|\Psi\rangle_{12} \xrightarrow{\hat{\theta}_2} |\Psi\rangle_1 = \frac{1}{\sqrt{2}} \cos\theta_2|mV\rangle_1 + \frac{1}{\sqrt{2}} \sin\theta_2|-mH\rangle_1 \quad (3)$$

its normalized state is  $\cos\theta_2|mV\rangle_1 + \sin\theta_2|-mH\rangle_1$ , where  $\theta_2 = \{0^\circ, 45^\circ, 90^\circ, 135^\circ\}$ . When photon 2 is projected onto the basis  $\theta_2 = 0^\circ$  or  $\theta_2 = 90^\circ$ , the OAM information of photon 1 becomes determinable, and no interference will be observed. Conversely, when photon 2 is projected onto the basis  $\theta_2 = 45^\circ$  or  $\theta_2 = 135^\circ$ , the hybrid entangled system retains distinguishable information, and interference will be absent. This is because the OAM information of photon 1 is still marked by different polarization states, indicating that the which-path (which-OAM) information is not fully erased.

To fully erase the which-OAM information, we insert a polarizer 1 in the path of photon 1, which can project the polarization of photon 1 onto the following state:

$$|\theta_1\rangle_1 = \cos\theta_1|H\rangle_1 + \sin\theta_1|V\rangle_1 \quad (4)$$

Combining Equations (3) and (4), we will obtain:

$$|\Psi\rangle_1 \xrightarrow{\hat{\theta}_1} \frac{1}{\sqrt{2}} \sin\theta_1 \cos\theta_2|m\rangle_1 + \frac{1}{\sqrt{2}} \cos\theta_1 \sin\theta_2|-m\rangle_1 \quad (5)$$

Letting  $r = 1/\sqrt{|\sin\theta_1 \cos\theta_2|^2 + |\cos\theta_1 \sin\theta_2|^2}$ , then the normalized form of the above state is  $(\sin\theta_1 \cos\theta_2/r)|m\rangle_1 + (\cos\theta_1 \sin\theta_2/r)|-m\rangle_1$ . This implies that when photon 2 is projected onto the state  $\theta_2 = 0^\circ$  or  $\theta_2 = 90^\circ$ , photon 1 owns definitive OAM information ( $m$  or  $-m$ ), hence no interference petal-like patterns will be observed; however, when photon 2 is projected onto the state  $\theta_2 = 45^\circ$  or  $\theta_2 = 135^\circ$ , the which-OAM information of photon 1 can be fully erased by choosing an appropriate  $\theta_1$  for polarizer 1. In the latter scenario, by setting  $\theta_1 = 0^\circ$  or  $\theta_1 = 90^\circ$ , the which-OAM information will be tagged, and no interference occurs; instead, a quantum eraser can be achieved by setting  $\theta_1 = 45^\circ$  or  $135^\circ$ , since any photon 1 transmitted through the polarizer 1 is likely to be in the superposition state of the OAM, resulting in the appearance of interference petal-like patterns.

The traditional approaches for detecting OAM states require exhaustive detection of all possible OAM modes via mode switching. It takes thousands of photons to identify each mode, which is highly inefficient. Here, we directly correlate the spatial distribution of photon 1 with counts of photon 2 to observe the disappearance and reappearance of interference petal-like OAM

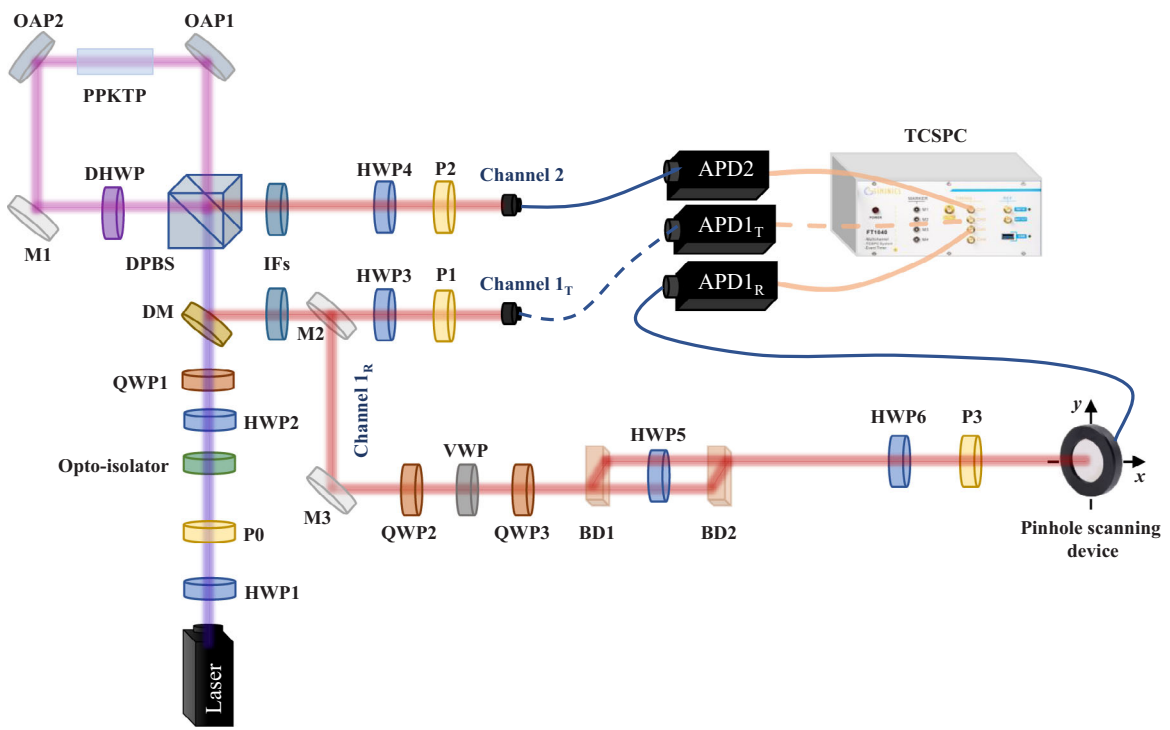


**FIGURE 1** | Experimental setup for our hybrid entanglement quantum erasure. The entangled photon pairs were generated by pumping a periodically poled potassium titanyl phosphate (PPKTP) crystal in a rectangular asymmetric interferometer and encoded to produce a hybrid entangled state. The half-wave plate (HWP) and polarizer assemblies (HWP3-P1, HWP4-P2 and HWP6-P3) were applied to make measurements, which were recorded by avalanche photodiodes (APDs), followed by a time-correlated single-photon counting (TCSPC) device to produce the coincidence counts. HWP: half-wave plate, P: polarizer, QWP: quarter-wave plate, DM: dichroic mirror, DPBS: dual-wavelength polarizing beam splitter, DHWP: dual-wavelength half-wave plate, M: mirror, OAP: off-axis parabolic mirror, PPKTP: periodically poled potassium titanyl phosphate, IF: interference filter, VWP: vortex wave plate, BD: beam displacer.

patterns. To visualize this hybrid entanglement quantum erasure, we propose a first-photon imaging method based on a physics-enhanced neural network. The total number of photons used for image reconstruction is reduced to only a few thousand. The details of the algorithm will be elaborated later.

### 3 | Experimental Setup

The experimental setup (Figure 1) consisted of an entangled photon source integrated with a polarization-orbital angular momentum (OAM) hybrid entanglement encoder and measurement module. Our type-II spontaneous parametric down-conversion (SPDC) source employed a rectangular asymmetric interferometer design [37], where a 405 nm continuous-wave laser beam passed sequentially through a half-wave plate (HWP1) and polarizer P0 for intensity adjustment, followed by HWP2 and quarter-wave plate (QWP1) for phase modulation. A dichroic mirror (DM) separated the 405 nm pump light from the generated 810 nm entangled photon pairs. Within the interferometer, a dual-wavelength PBS directed the pump beam to three essential components: (1) a periodically poled potassium titanyl phosphate (PPKTP) nonlinear crystal, (2) two off-axis parabolic mirrors focusing the pump onto the PPKTP crystal center, and (3) a dual-wavelength half-wave plate (DHWP) for polarization state conversion. Operating at 10 mW pump power, the system achieved single-photon detection rates of  $798 \times 10^3$  and  $800 \times 10^3$  counts  $s^{-1}$  in the two output channels, with a coincidence

count rate of  $105 \times 10^3$  counts  $s^{-1}$ , corresponding to a photon pair generation efficiency of  $10.5 \times 10^3$  counts  $s^{-1}$  mW $^{-1}$ . All detections were time-tagged with a 64 ps bin (Siminics FT1040), forming a time histogram of 150 bins spanning 9.6 ns. The avalanche photodiode (APD) modules (Excelitas SPCM-800-14-FC, dark count rate  $\approx 100$  s $^{-1}$ ) exhibit a timing resolution  $\approx$  350 ps full width at half maximum (FWHM) (root mean square (RMS)  $\approx 150$  ps) and a dead time of 22 ns. We retain the full per-pixel time histogram as the temporal dimension of our 4D data (see Section 4), allowing the reconstruction network to enforce coincidence-consistent timing constraints. This space-time representation enables reliable coincidence identification and effective discrimination of independent photons between channels in continuous measurements.

For polarization entanglement characterization, we inserted waveplate-polarizer pairs HWP3-P1 and HWP4-P2 into channels 1<sub>T</sub> and 2, respectively. The interferometer's design effectively suppressed single-photon interference, ensuring that all observed interference patterns resulted exclusively from two-photon quantum interference. This characteristic fundamentally differentiates our quantum erasure experiments from classical optical implementations. Polarization correlation measurements revealed visibilities of 98% in the H/V basis ( $\theta_1 = 0^\circ/90^\circ$ ) and 97% in the D/A basis ( $\theta_1 = 45^\circ/135^\circ$ ), as shown in Figure 2. These high visibility values demonstrate the excellent quality of our entangled photon source. In the experiment, the polarization-entangled photon source at the outputs of the interferometer was

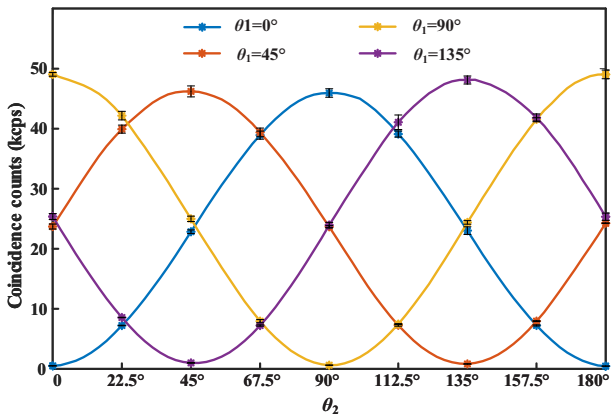


**FIGURE 2** | Coincidence counts as a function of  $\theta_2$  when  $\theta_1 = 0^\circ$ ,  $45^\circ$ ,  $90^\circ$ , and  $135^\circ$ , where  $\theta_1$  and  $\theta_2$  were the polarization bases of channel 1<sub>T</sub> and channel 2, respectively.

prepared in a certain state

$$|\Psi\rangle'_{12} = \frac{1}{\sqrt{2}}(|H\rangle_1|V\rangle_2 + |V\rangle_1|H\rangle_2) \quad (6)$$

An effective method to accurately assess the polarization-entangled states generated in our experiment is to measure the fidelity, defined as  $F(\rho, \sigma) = \text{Tr } \sqrt{\rho^{1/2}\sigma\rho^{1/2}}$ , where Tr denotes the trace,  $\rho$  represents the density matrix of the theoretical state  $|\Psi\rangle'_{12}$  and  $\sigma$  denote the experimentally reconstructed density matrix. Our measurements yielded a fidelity of 97.9% for the polarization-entangled state. Following this source characterization, a QWP-VWP-QWP sandwich configuration was used to convert the Gaussian wavefront into a vortex wavefront, thereby preparing the polarization-OAM hybrid state. The optical components employed here have the following specifications: each QWP (LBTEK AQWP25-SNIR-A-M) has a retardance tolerance of  $\pm\lambda/80$  at 810 nm and a fast-axis accuracy of  $\pm3^\circ$ , while the VWP (LBTEK VR2-808) specifies a fast-axis accuracy of  $\pm1^\circ$  at 810 nm. Using the standard Poincaré-sphere description of linear retarders and the fidelity-angle relation on the Bloch sphere [44, 45], we could combine the manufacturer's tolerances with the measured polarization-state fidelity to achieve a lower bound of  $\gtrsim 97.2\%$  for the overall fidelity of the experimentally prepared hybrid entangled state.

We derived the channel 1<sub>R</sub> by using mirrors M2 and M3 and let photon 1 pass through the quarter-wave plate (QWP) QWP2 ( $45^\circ$ )-vortex wave plate (VWP)-QWP3 ( $-45^\circ$ ) to prepare the polarization-OAM state of photon 1. Then, the two-photon state could be expressed as

$$|\Psi\rangle''_{12} = \frac{1}{\sqrt{2}}(|-mV\rangle_1|V\rangle_2 + |mH\rangle_1|H\rangle_2) \quad (7)$$

Due to inevitable imperfections in the wave plates and polarizing beam splitters (PBSs), as well as a slight path-length mismatch, a non-ideal relative phase might be introduced between these two probability amplitudes. We used  $m$ -order VWP to convert the basic Gaussian mode  $|0\rangle$  into the OAM mode  $|m\rangle$  or  $| -m\rangle$ , where  $|m\rangle_1$  ( $| -m\rangle_1$ ) denoted photon 1 going the up (down) path (it could be done by using the beam displacer (BD) BD1).

Inserting an HWP5 ( $45^\circ$ ) in both up and down paths after BD1 could initialize photon 1 in the up and down paths to the horizontal and vertical polarizations, respectively. After the beam recombination at BD2, the two paths formed an interferometer. By finely tuning the relative phase to 0, we successfully prepared a hybrid entangled state of the polarization-OAM DOF of photon 1 and the polarization DOF of photon 2

$$|\Psi\rangle_{12} = \frac{1}{\sqrt{2}}(|-mH\rangle_1|V\rangle_2 + |mV\rangle_1|H\rangle_2) \quad (8)$$

After BD2, we used HWP6 and P3 to measure the polarization state of photon 1, similar to the role of HWP4 and P2 in channel 2. A 2D pinhole scanning device was placed after P3 for transverse probing the first arriving photon at each spatial position in channel 1<sub>R</sub>. At last, the signal photons from channels 1<sub>R</sub> and 2 were fed through the single mode fibers (SMFs) to the APD1<sub>R</sub> and APD2 for coincidence counting within 2 ns gating time of the time-correlated single-photon counting (TCSPC) device.

#### 4 | Acquisition of 4D Single-Photon Data and Reconstruction Network

In conventional first-photon or photon-efficient algorithms, the laser pulse signal served as the trigger, and the first returning photon was recorded as the stop to determine the time of flight (TOF). By dividing the TOF by the laser pulse period  $T_r$ , the number of emitted pulses,  $N_e$ , was determined, and its reciprocal was used for image reconstruction. However, in this experiment, there was no pulse signal to serve as a trigger. Noting that the entangled photons generated by SPDC appeared in pairs at the same time, we subtly used photon 2 as the trigger (start) signal, and the first arriving photon detected at each spatial position in channel 1<sub>R</sub> as the stop signal, to form a 3D data cube. It could be further combined with the photon time distribution characteristics (i.e., TOF histograms) of the entangled light source to acquire 4D data.

Here we present FPDRANet, a first-photon physics-enhanced dual-branch residual attention network that leverages quantum entanglement properties for enhanced image reconstruction (Figure 3a). The architecture processes the prepared 4D raw data through two specialized pathways designed for complementary feature extraction. The network's asymmetric architecture consists of parallel processing streams with distinct functional roles. The upper pathway focuses on single-channel intensity feature analysis using three Residual Attention Blocks (RABs) arranged in a U-shaped configuration. This design integrates spatial resolution adaptation with squeeze-and-excitation attention mechanisms to preserve critical intensity information. Conversely, the lower pathway handles high-dimensional temporal features across 2000 channels through four Hybrid Dense Residual Attention Blocks (HDRABs), which employ dense inter-layer connections to facilitate complex feature transformations. Both processing streams converge through identical projection layers that map features to a unified 150D representation space before final fusion. This dual-branch approach maintains consistent spatial dimensions in the intensity pathway while preserving original feature characteristics in the temporal pathway. The complete system achieves computational efficiency through balanced

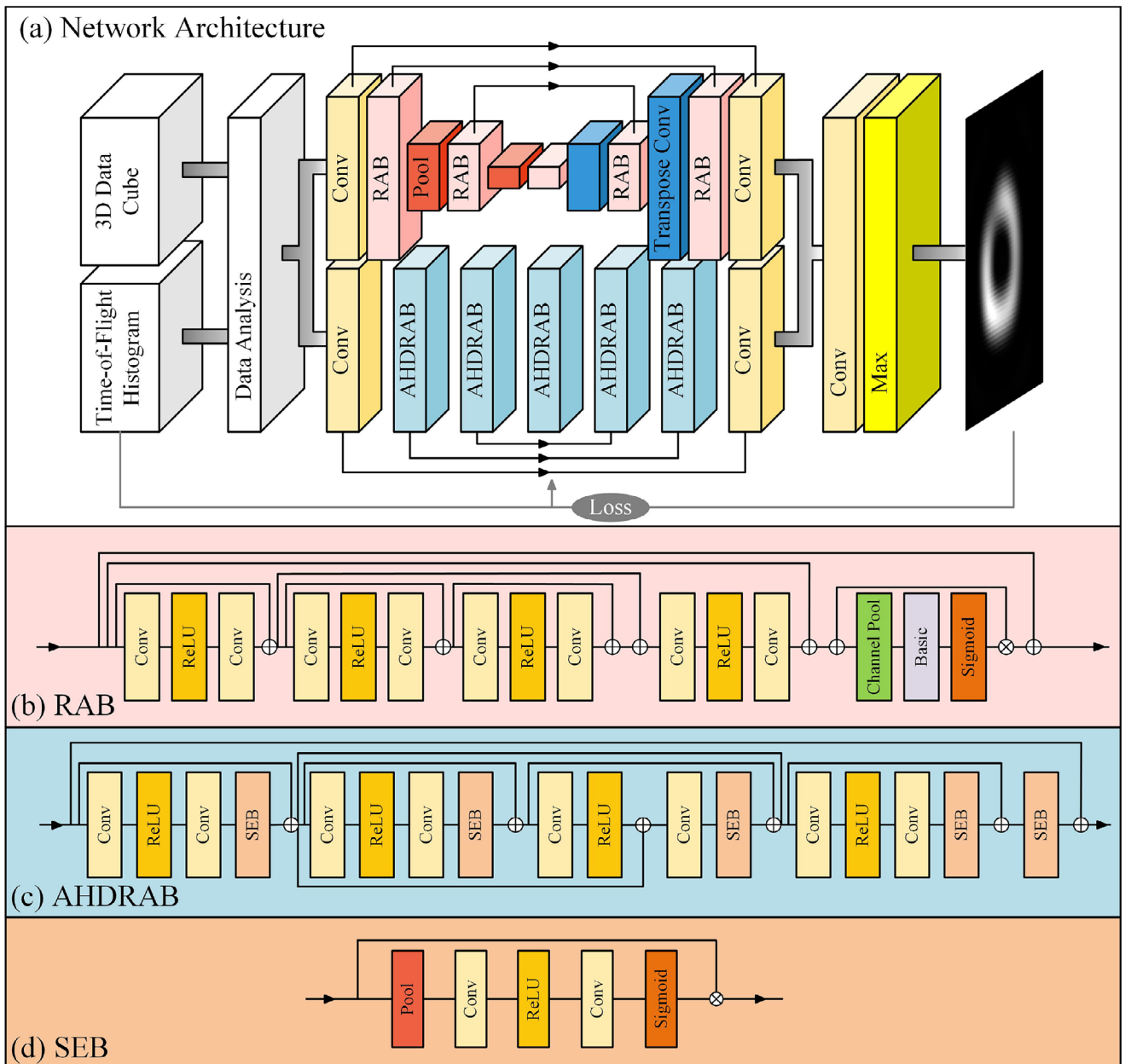


**FIGURE 3** | Architecture of first-photon physics-enhanced dual-branch residual attention network. The upper branch extracts spatial intensity features using Residual Attention Blocks (RABs), while the lower branch captures temporal information through Hybrid Dense Residual Attention Blocks (AHDRAbs). Both branches incorporate attention mechanisms and project features to a unified space for fusion. The architecture is optimized for robust image reconstruction from photon-limited, high-dimensional data.

parameter distribution (4.50 M total parameters) and optimized FLOPs allocation (1: 352 ratio) between branches.

Both branches converge through structurally identical projection layers that map features to a unified 150-channel representation space prior to concatenation-based fusion. The network consistently applies residual learning principles throughout its architecture, with the upper branch maintaining consistent spatial dimensions via symmetrical downsampling/upsampling operations while the lower branch preserves the original feature dimensionality. Notable architectural innovations include the modality-specific RAB/AHDRAb designs that address distinct input characteristics and the shared projection layers

that ensure feature space compatibility before cross-branch interaction.

The RAB module (Figure 3b) implements spatially-optimized residual learning through a four-stage feature refinement process. Initial processing involves three sequential residual transformations that progressively increase feature complexity, followed by cross-stage feature aggregation that combines shallow and deep representations. Subsequent processing includes additional residual refinement and spatial attention modulation, where  $5 \times 5$  convolutional operations generate attention masks emphasizing critical regions through channel-wise pooling. This architecture preserves original input features through residual connections

while adaptively enhancing semantically significant regions, achieving effective gradient propagation across four transformation levels and three skip connections.

HDRAB modules (Figure 3c) employ a hierarchical architecture that combines multi-scale dilated convolutions (rates 1–4) with dual attention mechanisms. The bottom-up processing path utilizes progressively increasing dilation rates coupled with SEBlock attention modules, while the top-down path implements feature aggregation through additive skip connections. Final feature optimization incorporates both channel attention mechanisms and global residual learning. All convolutional operations maintain spatial dimensions through  $3 \times 3$  kernels with dilation-appropriate padding, using ReLU activation throughout except in SEBlock (Figure 3d) gating components. This design simultaneously achieves three complementary objectives: multi-scale context integration through configurable dilation rates, channel-wise feature recalibration via attention mechanisms, and efficient feature reuse through dense cross-scale connections.

We experimentally acquired single-photon OAM data using a combination of SPAD and TCSPC. With an integration time of 1–10 s per pixel, we partitioned photon events along the temporal axis and constructed 4D data cubes—containing 1200 training samples and 400 testing samples based on the methods mentioned above. These cubes enabled first-photon image reconstruction, which specifically incorporates first-photon ToF information and the corresponding first-photon event distribution characteristics recorded at each pixel location. Each data cube has a spatial resolution of  $64 \times 64$  and a temporal axis with 150 time bins. The dataset includes 16 OAM image categories. We trained the designed network (FPDRANet) using the training data and evaluated its performance with the testing data. The FPDRA-Net was optimized via the Adam optimizer (learning rate = 0.001), with its composite loss function integrating three key metrics: mean squared error (MSE) for intensity fidelity, structural similarity (SSIM) for spatial feature preservation, and Kullback-Leibler (KL) divergence for photon statistics matching:

$$L = L_{\text{MSE}} + \zeta L_{\text{SSIM}} + \eta L_{\text{KL}} \quad (9)$$

$$L_{\text{MSE}}(\hat{O}, O) = \|\hat{O} - O\|^2 \quad (10)$$

$$L_{\text{SSIM}} = 1 - \frac{(2\mu_x\mu_y + C_1)(2\sigma_x\sigma_y + C_2)}{(\mu_x^2 + \mu_y^2 + C_1)(\sigma_x^2 + \sigma_y^2 + C_2)} \quad (11)$$

$$L_{\text{KL}} = \sum_i^N p(x_i) \cdot \log \frac{p(x_i)}{q(x_i)} \quad (12)$$

where  $\hat{O}$  and  $O$  represented the reconstructed data and ground truth,  $p(x_i)$  and  $q(x_i)$  stood for the recovered TOF histogram and ground truth, the parameters  $\zeta$  and  $\eta$  were the weights with very small values,  $\mu_x$  and  $\mu_y$  denoted the mean grayscale values,  $\sigma_x$  and  $\sigma_y$  were the standard deviations,  $C_1$  and  $C_2$  were small constants to avoid zero in the denominator. This multi-

term optimization strategy ensures simultaneous reconstruction accuracy and physical consistency. The training was carried out on a computer equipped with an Intel i9-14900HX processor and an NVIDIA GTX 4060 graphics card, taking 4 to 5 h to complete.

## 5 | Reconstruction Results and Comparative Analysis

To validate the effectiveness of the FPDRA-Net in image reconstruction, we projected photon 1 onto the state  $|D\rangle_1$  (or  $|V\rangle_1$ ) and photon 2 onto the state  $|D\rangle_2$ . We used the images recovered by the original first-photon algorithm SPIRAL-TAP [28] for comparison. Figure 4 presents comparative results of raw data and reconstructed images under different quantum state configurations. Figure (4a) and (c) display experimental data when both photons 1 and 2 are in the  $|D\rangle$  state: (a) shows photon time distribution characteristics based on entangled photon pair counting (analogous to pulse number statistics in conventional first-photon algorithms), while (c) presents the 2D distribution of first-photon time-of-flight detection. Figure (4e) and (g) demonstrate reconstruction results from SPIRAL-TAP algorithm and our FPDRA-Net respectively, with (i) showing the reference intensity distribution at 10 s  $\text{pixel}^{-1}$  integration. Quantitative analysis reveals FPDRA-Net's superior performance in (g) with  $\text{MSE} = 0.0041$  and  $\text{SSIM} = 0.8262$  (annotated at bottom-right). Figure (4b) and (d) present experimental data when photon 1 is in  $|V\rangle_1$  state and photon 2 is in the  $|D\rangle_2$  state: (b) shows photon time distribution characteristics, while (d) displays corresponding time-of-flight distribution. Among reconstruction results (f) and (h), the FPDRA-Net achieves metrics in (h) with  $\text{MSE} = 0.0069$  and  $\text{SSIM} = 0.8367$ . (j) provides reference image under identical conditions with (i). All reconstructions (e-h) use extremely low sampling ( $0.7656 \text{ photons pixel}^{-1}$ ) at  $64 \times 64$  pixel resolution. These experiments demonstrate that under sub-Poissonian entangled-photon flux ( $0.7656 \text{ photon pixel}^{-1}$ ) and appreciable ambient noise, the conventional SPIRAL-TAP algorithm fails to recover image structure. This is consistent with its modeling assumptions (pulsed illumination, independent Poisson arrivals), which are mismatched to our heralded, continuous-wave entangled acquisition with non-negligible accidental noise. By contrast, the FPDRA-Net is explicitly aligned with the measurement physics: the idler heralds the start, and the first detected signal at each  $(x, y)$  defines a per-pixel first-photon ToF histogram  $H(x, y, t)$ ; together with the source timing profile  $h(t)$ , this yields a 4D representation  $(x, y, t; h)$ , on which coincidence-consistent timing constraints are enforced. A spatial branch captures the  $2|m|$ -petal OAM symmetries, while a temporal branch models coincidence statistics; their fusion acts as a correlation-aware matched estimator that suppresses uncorrelated background and preserves petal structure. Consequently, the FPDRA-Net reconstructs the OAM patterns with high fidelity at low flux, achieving SSIMs of 0.8262 and 0.8367 in Figure 4, thereby enabling reliable visualization of quantum erasure in the polarization OAM hybrid entangled system.

We systematically prepared photon pairs in four distinct polarization states ( $|H\rangle$ ,  $|V\rangle$ ,  $|D\rangle$ , and  $|A\rangle$ ) and employed our FPDRA-Net architecture for first-photon image reconstruction (Figure 5). Quantitative analysis revealed an average photon consumption of 0.6404 photons per pixel for reconstructing

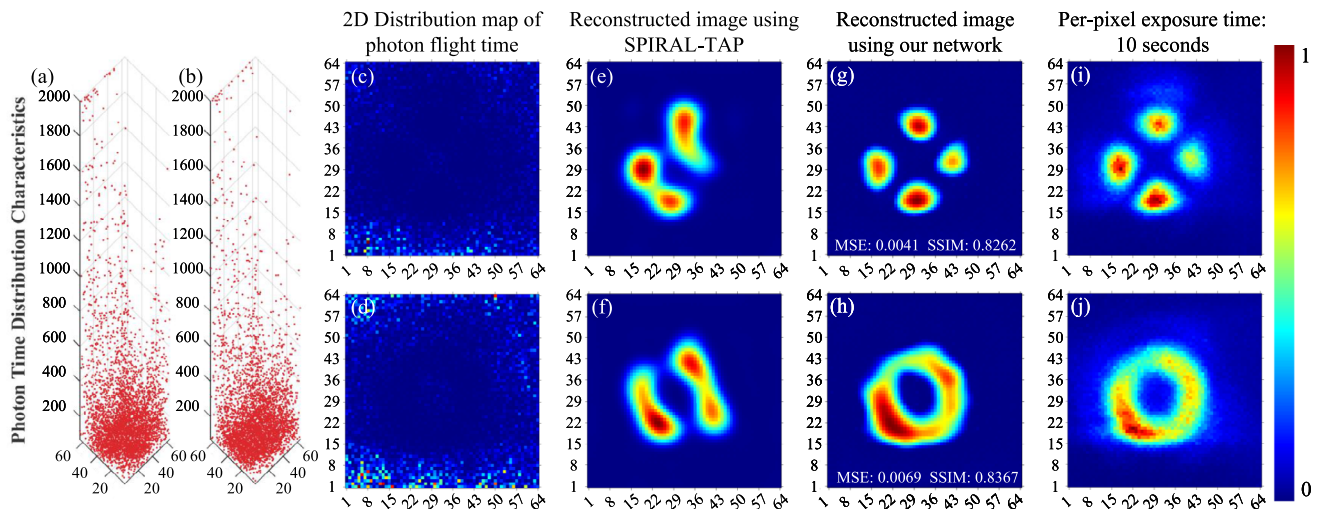


**FIGURE 4** | Comparative image reconstruction performance between SPIRAL-TAP algorithm and the proposed network. (a,c) Raw data for reconstruction when both photons 1 and 2 are in  $|D\rangle$  state: (a) photon time distribution characteristics; (c) first-photon time-of-flight. (e,g) Reconstruction results from SPIRAL-TAP and our network, respectively. (i) Reference image obtained with  $10\text{ s pixel}^{-1}$  integration. (b,d) Corresponding raw data when photon 1 is in  $|V\rangle_1$  and photon 2 in  $|D\rangle_2$  state. (f,h) Respective reconstructions from SPIRAL-TAP and our method. (j)  $10\text{ s pixel}^{-1}$  reference image. All images have  $64 \times 64$  pixel resolution. Reconstructions in (e–h) used input data with identical photon flux ( $0.7656\text{ photons pixel}^{-1}$ ). Each panel labels the sign of the OAM index  $m$  (e.g.,  $|m = +2\rangle$ ,  $|m = -2\rangle$ , and  $|m = \pm 2\rangle$  for superpositions).

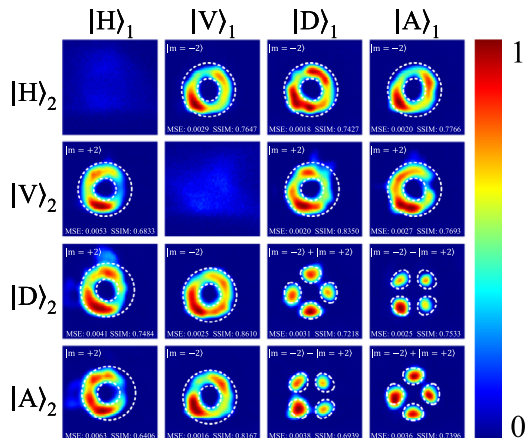


**FIGURE 5** | Intensity images reconstructed by our network in the quantum erasure experiment, all of  $64 \times 64$  pixels, with an average of  $0.6404\text{ photons per pixel}$ . The states of photon 1 were denoted as  $|H\rangle_1$ ,  $|V\rangle_1$ ,  $|D\rangle_1$ , and  $|A\rangle_1$ , while the states of photon 2 were indicated by  $|H\rangle_2$ ,  $|V\rangle_2$ ,  $|D\rangle_2$ , and  $|A\rangle_2$ . Each panel labels the sign of the OAM index  $m$  (e.g.,  $|m = +2\rangle$ ,  $|m = -2\rangle$ , and  $|m = \pm 2\rangle$  for superpositions).

valid sub-images, excluding cases where both photons were in  $|H\rangle$  or  $|V\rangle$  states. Each reconstructed image was evaluated against its corresponding  $10\text{ s}$  exposure reference (averaging  $9.15\text{ photons pixel}^{-1}$ ) by computing MSE and SSIM metrics, with values annotated at the lower-right corner. The experimental results demonstrated remarkable consistency with theoretical predictions, as evidenced by the quantitative similarity metrics. Through polarization state selection, we observed controllable disappearance and reappearance of characteristic petal-like interference patterns. This confirms that active polarization manipulation via linear polarizers enables quantum erasure of the interference structures.

## 6 | Conclusion

In this work, we present a quantum erasure experimental scheme based on polarization-OAM two-photon hybrid entanglement. This scheme constructs inseparable polarization-OAM coupled states for a signal photon, with two linear polarizers placed in separate detection arms serving as quantum erasers. Leveraging the developed FPDRANet, we successfully visualize the disappearance and reappearance of interference petal-like patterns with an average of fewer than one photon per pixel, dispensing with the need for exhaustive detection of all OAM modes. The results have demonstrated that the interference petal-like patterns can be effectively erased through precise polarization control of the linear polarizers. This visualization approach not only sheds new light on the fundamental issue of quantum mechanics, but also widens the boundaries of quantum imaging technology.

Looking ahead, our first-photon quantum-imaging framework, which recovers high-dimensional OAM information from 4D time-tagged data under sub-photon flux, can be directly interfaced with OAM-encoded qudit architectures in integrated photonics processors. This enables efficient state preparation and fast readout without the need for exhaustive mode scanning. Such a capability simplifies low signal-to-noise ratio (SNR) calibration and verification of high-dimensional quantum gates, facilitates resource-aware tomography and device characterization, and offers a scalable pathway toward larger optical quantum computing platforms. Furthermore, representing high-dimensional quantum information as images provides an intuitive diagnostics layer for complex photonic quantum circuits, helping to bridge classical imaging tools with quantum operations. In summary, the proposed approach serves as a stepping stone toward scalable and measurement-efficient control of high-dimensional photonic quantum systems.

## Author Contributions

A.N.Z., X.X.C., and J.Z.Y. proposed the idea. W.K.Y., Q.Y.W., X.X.C., J.H., J.L., and J.Z.Y. performed the experiments. Q.Y.W. and X.X.C. curated the data. Q.Y.W., X.X.C., and W.K.Y. wrote the original draft. W.K.Y. and A.N.Z. reviewed and edited the manuscript. A.N.Z. and W.K.Y. supervised the project. All authors discussed the results and approved the final manuscript. W.K.Y., X.X.C., and Q.Y.W. contributed equally and are co-first authors.

## Acknowledgements

This work was supported by the National Natural Science Foundation of China (Grant Nos. 92365115, 12474480, and 62571047).

## Conflicts of Interest

The authors declare no conflicts of interest.

## Data Availability Statement

The full source code is accessible at <https://github.com/qingyuanwu/FPDRANet>. All data necessary to evaluate the conclusions of this work are provided in the paper.

## References

- M. O. Scully and K. Drühl, "Quantum Eraser: A Proposed Photon Correlation Experiment Concerning Observation and "Delayed Choice" in Quantum Mechanics," *Physical Review A* 25 (1982): 2208.
- M. O. Scully, B.-G. Englert, and H. Walther, "Quantum Optical Tests of Complementarity," *Nature* 351 (1991): 111.
- Y.-H. Kim, R. Yu, S. P. Kulik, Y. Shih, and M. O. Scully, "Delayed "Choice" Quantum Eraser," *Physical Review Letters* 84 (2000): 1.
- S. P. Walborn, M. O. T. Cunha, S. Pádua, and C. H. Monken, "Double-Slit Quantum Eraser," *Physical Review A* 65 (2002): 033818.
- R. Ionicioiu and D. R. Terno, "Proposal for a Quantum Delayed-Choice Experiment," *Physical Review Letters* 107 (2011): 230406.
- J. S. Tang, Y. L. Li, X. Y. Xu, G. Y. Xiang, C. F. Li, and G. C. Guo, "Realization of Quantum Wheeler's Delayed-Choice Experiment," *Nature Photonics* 6 (2012): 600.
- F. Kaiser, T. Coudreau, P. Milman, D. B. Ostrowsky, and S. Tanzilli, "Entanglement-Enabled Delayed-Choice Experiment," *Science* 338 (2012): 637.
- K. Wang, Q. Xu, S. Zhu, and X. S. Ma, "Quantum Wave-Particle Superposition in a Delayed-Choice Experiment," *Nature Photonics* 13 (2019): 872.
- J. Li, X. X. Chen, Z. Meng, et al., "Superposition-State Generation of Nonorthogonal Wavelike and Particlelike States Without Ancillary Qubits," *Physical Review A* 108 (2023): 022221.
- L. Chen, W. Zhang, K. Cai, Y. Zhang, and Q. Qi, "Revisiting the Which-Way Experiment With Twisted Light Beams," *Optics Letters* 39 (2014): 5897.
- I. Nape, B. Ndagano, and A. Forbes, "Erasing the Orbital Angular Momentum Information of a Photon," *Physical Review A* 95 (2017): 053859.
- M. Kolář, T. Opatrný, and G. Kurizki, "Path and Phase Determination for an Interfering Photon With Orbital Angular Momentum," *Optics Letters* 33 (2008): 67.
- I. Nape, C. Kyeremah, A. Vallés, C. Rosales-Guzmán, P. K. Buah-Bassuah, and A. Forbes, "A Hybrid Quantum Eraser Scheme for Characterization of Free-Space and Fiber Communication Channels," *Optics Communications* 408 (2018): 53.
- X. Qiu, H. Guo, and L. Chen, "Remote Transport of High-Dimensional Orbital Angular Momentum States and Ghost Images via Spatial-Mode-Engineered Frequency Conversion," *Nature Communications* 14 (2023): 8244.
- L. Allen, M. W. Beijersbergen, R. J. C. Spreeuw, and J. P. Woerdman, "Orbital Angular Momentum of Light and the Transformation of Laguerre-Gaussian Laser Modes," *Physical Review A* 45 (1992): 8185.
- T. Stav, A. Faerman, E. Maguid, et al., "Quantum Entanglement of the Spin and Orbital Angular Momentum of Photons Using Metamaterials," *Science* 361 (2018): 1101.
- E. Otte, C. Rosales-Guzmán, B. Ndagano, C. Denz, and A. Forbes, "Entanglement Beating in Free Space Through Spin-Orbit Coupling," *Light: Science & Applications* 7 (2018): 18009.
- Y. Shen, X. Wang, Z. Xie, et al., "Optical Vortices 30 Years On: OAM Manipulation From Topological Charge to Multiple Singularities," *Light: Science & Applications* 8 (2019): 90.
- R. Horodecki, P. Horodecki, M. Horodecki, and K. Horodecki, "Quantum Entanglement," *Reviews of Modern Physics* 81 (2009): 865.
- E. Nagali, F. Sciarrino, F. D. Martini, et al., "Quantum Information Transfer From Spin to Orbital Angular Momentum of Photons," *Physical Review Letters* 103 (2009): 013601.
- J.-W. Pan, Z.-B. Chen, C.-Y. Lu, H. Weinfurter, A. Zeilinger, and M. Żukowski, "Multiphoton Entanglement and Interferometry," *Reviews of Modern Physics* 84 (2012): 777.
- E. Bagan, J. A. Bergou, S. S. Cottrell, and M. Hillery, "Relations Between Coherence and Path Information," *Physical Review Letters* 116 (2016): 160406.
- P. Lipka-Bartosik, H. Wilming, and N. H. Y. Ng, "Catalysis in Quantum Information Theory," *Reviews of Modern Physics* 96 (2024): 025005.
- X. Y. Zou, L. J. Wang, and L. Mandel, "Induced Coherence and Indistinguishability in Optical Interference," *Physical Review Letters* 67 (1991): 318.
- X.-X. Chen, Q.-Y. Wu, Z. Meng, et al., "Imaging of Single-Photon Orbital-Angular-Momentum Bell States," *Physical Review Applied* 18 (2022): 054053.
- M. Aili, X.-X. Chen, P. Liu, et al., "Characterizing Interference Effects of Vortex Beams Based on the Sagnac Interferometer," *Physical Review A* 106 (2022): 023715.
- M. Aili, P. Liu, X.-X. Chen, et al., "Double-Slit Experiment With Multiple Vortex Beams," *Physical Review A* 109 (2024): 013521.
- A. Kirmani, D. Venkatraman, D. Shin, et al., "First-Photon Imaging," *Science* 343 (2014): 58.
- X. Liu, J. Shi, X. Wu, and G. Zeng, "Fast First-Photon Ghost Imaging," *Scientific Reports* 8 (2018): 5012.
- X. Peng, X.-Y. Zhao, L.-J. Li, and M.-J. Sun, "First-Photon Imaging via a Hybrid Penalty," *Photonics Research* 8 (2020): 325.
- Y. Cheng, X.-Y. Zhao, L.-J. Li, and M.-J. Sun, "First-Photon Imaging With Independent Depth Reconstruction," *APL Photonics* 7 (2022): 036103.
- Z. Li, X. Liu, J. Wang, Z. Shi, L. Qiu, and X. Fu, "Fast Non-Line-of-Sight Imaging Based on First Photon Event Stamping," *Optics Letters* 47 (2022): 1928.
- J. H. Shapiro, "First-Photon Target Detection: Beating Nair's Pure-Loss Performance Limit," *Physical Review A* 106 (2022): 032415.
- D. Shin, A. Kirmani, V. K. Goyal, and J. H. Shapiro, "Photon-Efficient Computational 3-D and Reflectivity Imaging With Single-Photon Detectors," *IEEE Transactions on Computational Imaging* 1 (2015): 112.
- D. Shin, F. Xu, D. Venkatraman, et al., "Photon-Efficient Imaging With a Single-Photon Camera," *Nature Communications* 7 (2016): 12046.
- J. Rapp and V. K. Goyal, "A Few Photons Among Many: Unmixing Signal and Noise for Photon-Efficient Active Imaging," *IEEE Transactions on Computational Imaging* 3 (2017): 445.

37. Z. Meng, J. Yang, J. Li, X. Chen, Q. Wu, and A. Zhang, "AI Polarization Compensation Algorithm Using an Asymmetry Entangled Photon Source," *Physica Scripta* 98 (2023): 125105.
38. Z. Wu, R. Gao, S. Zhou, et al., "Robust Super-Resolution Image Transmission Based on a Ring-Core Fiber With Orbital Angular Momentum," *Laser & Photonics Reviews* 18 (2023): 2300624.
39. S. Geng, P. Xu, Y. Sun, et al., "Design and Experimental Research of Orbital Angular Momentum Multiplexing Holography Based on Optical Diffraction Neural Network," *Optics Express* 32 (2024): 33716.
40. Z.-G. Zheng, F.-F. Han, L. Wang, and S.-M. Zhao, "Generation of Orbital Angular Momentum Hologram Using a Modified U-Net," *Chinese Physics B* 33 (2024): 034207.
41. N. Asoudegi and M. Mojahedi, "Orbital Angular Momentum Holography Using Neural Network and Camera in the Loop," *Laser & Photonics Reviews* 19 (2025): e00224.
42. J. Liu, Z. Liang, J. Chen, et al., "Dual-Parameter Encoded Orbital Angular Momentum Mode Multiplexing Holography Using Rotatable Diffractive Neural Networks," *Journal of Lightwave Technology* 43 (2025): 8225.
43. C. Xing, X. Tong, S. Liu, P. Xu, and D. Zhao, "3D Light-Field Reconstruction With Single Shot Based on Radially Self-Accelerating Beams," *Laser & Photonics Reviews* 19 (2025): e00362.
44. R. M. A. Azzam, "Poincaré Sphere Representation of the Fixed-Polarizer Rotating-Retarder Optical System," *Journal of the Optical Society of America A* 17 (2000): 2105.
45. M. A. Nielsen and I. L. Chuang, *Quantum Computation and Quantum Information* (Cambridge University Press, Cambridge, 2010).